

# Fourier-domain holographic optical coherence imaging of tumor spheroids and mouse eye

Kwan Jeong, Leilei Peng, John J. Turek, Michael R. Melloch, and David D. Nolte

Fourier-domain holography (FDH) has several advantages over image-domain holography for optical coherence imaging of tissue. Writing the hologram in the Fourier plane significantly reduces background arising from reference light scattered from the photorefractive holographic film. The ability to use FDH is enhanced by the use of a diffuse target, such as scattering tissue, rather than specular targets, because the broader angular distribution from diffuse targets is transformed into a relatively uniform distribution in the Fourier plane. We demonstrate significantly improved performance for Fourier-domain optical coherence imaging on rat osteogenic sarcoma tumor spheroids and mouse eye. The sensitivity is documented at  $-95$  dB. © 2005 Optical Society of America

OCIS codes: 170.1650, 070.2580, 190.5970, 030.6140, 090.0090.

## 1. Introduction to Optical Coherence Imaging

The extension of optical coherence-domain reflectometry<sup>1,2</sup> to optical coherence imaging (OCI) was first accomplished by the group at Imperial College using dynamic photorefractive media.<sup>3,4</sup> Holographic recording in photorefractive media performs as a coherence gate that eliminates diffuse glare from the image-bearing light. This approach is in principle background free and permits direct imaging, without computed reconstruction, through model turbid media to acquire *en face* images at a fixed depth<sup>5-7</sup> complementary to the point-scanning optical coherence tomography (OCT) techniques.<sup>8-10</sup> Because of the large pixel number of CCD cameras and their high sensitivity and hence short exposure time, the OCI approach has the potential for high-speed imaging.<sup>6,11,12</sup> The first OCI images inside living tissue were obtained from rat osteogenic tumor spheroids<sup>13,14</sup> that were of sizes ranging from 200- $\mu$ m to 1-mm diameter and were investigated under varying conditions that included exposure to metabolic drugs. The OCI approach was the first to use cellular motility

to differentiate between healthy specimens and metabolically altered specimens.<sup>15</sup>

The early research on holographic OCI, including the first images from living tissue, were all performed with image-domain holography (IDH), in which the holographic film was located at or near the image plane of the imaging optics. IDH was chosen, despite the acknowledged advantages of Fourier-domain holography (FDH),<sup>16-18</sup> because of the initial difficulty of establishing uniform Fourier intensity distributions at the holographic film when specular test charts are used.<sup>19</sup> The subsequent use of IDH for imaging through diffuse media made it extremely sensitive to dust and other imperfections on the holographic film that scattered reference light into the direction of the camera. Although background subtraction could remove much of the low-level scattered light, strong background from dust and imperfections saturated the camera, causing data dropout in the worst case and limiting the dynamic range of OCI in the best case.

These background problems (of a technique that is supposed to be background free) can be almost completely removed by conversion of the IDH system over to FDH. The key advantage of FDH (in which the holographic film is at the Fourier plane of the imaging optics) for the high-background OCI applications of tissue imaging is the removal of significant background scatter from the holographic film. This removal allows OCI to become background free in practice and opens the full dynamic range of the CCD camera for imaging into tissue. The key to this conversion was the recognition that diffuse targets such

---

The authors are with Purdue University, West Lafayette, Indiana. K. Jeong (jeongk@physics.purdue.edu), L. Peng, and D. Nolte are with the Physics Department; J. J. Turek is with the Department of Basic Medical Sciences; and M. R. Melloch is with the School of Electrical Engineering.

Received 21 July 2004; revised manuscript received 3 December 2004; accepted 5 December 2004.

0003-6935/05/101798-08\$15.00/0

© 2005 Optical Society of America

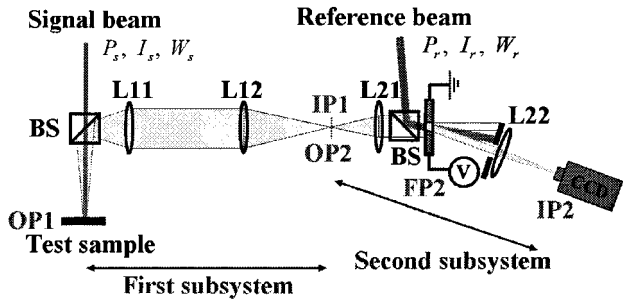


Fig. 1. Optical setup for FDH with two subsystems.  $P_s, P_r$ , powers;  $I_s, I_r$ , intensities;  $W_s, W_r$ , beam radii; BS, beam splitters; L11, L12, L21, L22, lenses; V, voltage; OP1, OP2, object planes; FP2, Fourier plane; IP1, IP2, image planes.

as tissue, unlike specular test charts that are commonly used for system alignment characterization, do produce relatively uniform intensity distributions at the Fourier plane, permitting uniform hologram recording in the photorefractive film.<sup>20</sup>

In this paper, we present the first results of FDH applied to OCI of tissue. The detailed description and analysis of FDH is presented in Section 2, followed by quantitative characterization of the system on diffuse (not specular) test charts in Section 3. In Section 4 the results are presented from tissue specimens: rat osteogenic sarcoma tumor spheroids and mouse eye. The key result from this section is the experimental demonstration of  $-95$ -dB sensitivity for FDH OCI, which is comparable with fast-scan time-domain OCT system sensitivities.

## 2. Optical Setup for Fourier-Domain Holography

The Fourier-domain holographic optical setup consists of two subsystems, the front-end system that conveys the object plane of the target to an intermediate image plane 1 (IP1) and the recording and read-out system that records a Fourier-domain hologram and images it to the CCD plane. These two subsystems are shown in Fig. 1 of the basic FDH system. IP1 is the object plane 2 (OP2) for the second subsystem. Fourier plane 2 (FP2) is located in the second subsystem, and final image plane 2 (IP2) is located at the CCD camera. In the system setup and analysis, the signal beam and the reference beam are assumed to be Gaussian beams. When the signal beam with intensity  $I_s$ , and radius  $W_s$  illuminates a volumetric diffuse test sample, the total coherent backscattered intensity  $I_{sO1}$  at object plane 1 (OP1) is

$$I_{sO1} \approx I_s \int_0^d R(z) \exp(-2\mu'z) dz \equiv B_s I_s, \quad (1)$$

where  $R(z)$  is the coherent reflectance per unit length at depth  $z$ ,  $\mu'$  is the reduced extinction coefficient of the sample, and  $d$  is the sample thickness. The backscattered power at OP1 is  $P_{sO1} = \pi I_{sO1} W_s^2 / 2$ . The image-bearing signal intensity  $I_{csO1}$  at OP1, which is matched to zero path with the reference beam, is

$$I_{csO1} \approx I_s R(z) l_c \exp(-2\mu'z) \equiv B_c I_s, \quad (2)$$

where  $l_c$  is the coherence length of laser. Equations (1) and (2) are valid only in the limit of small reflectance  $R(z)$  that neglects multiple scattering.

The optics collection efficiency  $\eta_c$  is the ratio of the collected amount to the total backscattered light and is

$$\eta_c = 2[1 - (1 - \sin^2 \theta_c)^{1/2}] \approx (\text{NA})^2$$

when the angular intensity of the coherent backscattered light varies approximately as  $\cos \theta$ . The numerical aperture of the collection optics is limited in practice by the width of the holographic film at the Fourier plane, which sets the maximum collection angle  $\theta_c$ . The collected beam power at object plane 2 (OP2) of subsystem 2 is given by  $P_{sO2} = \eta_c P_{sO1}$ . The intensity at FP2 of the second subsystem is

$$I_{sF2} = 2P_{sO2} / (\pi W_{sF2}^2),$$

where the beam radius at FP2 is  $W_{sF2} = (\text{NA})f_{21}/M_1$  and of which  $f_{21}$  is the focal length of the lens L21 and  $M_1$  is the magnification of the first subsystem. The intensity  $I_{sF2}$  at FP2 is then

$$I_{sF2} = B_s \frac{M_1^2 W_s^2 I_s}{f_{21}^2}. \quad (3)$$

The image-bearing intensity at FP2 is  $I_{csF2} = B_c I_{sF2} / B_s$ . When the hologram is written by signal intensity  $I_{sF2}$  and reference intensity  $I_r$ , the diffracted intensity  $I_{dF2}$  from the hologram is

$$I_{dF2} = \eta_p m^2 I_r = \eta_p \frac{4I_{csF2} I_r^2}{(I_r + I_{sF2})^2}, \quad (4)$$

where  $\eta_p$  is the maximum diffraction efficiency, and  $m$  is the modulation index. Maximum diffraction intensity occurs at the condition  $I_r = I_{sF2}$ , for which  $I_{dF2} = \eta_p I_{csF2}$ . The final intensity at image plane 2 (IP2) at the CCD camera is

$$I_{dI2} = I_{dF2} W_{dF2}^2 / W_{dI2}^2,$$

where the diffracted beam radius at IP2 is given by  $W_{dI2} = M W_s$  and  $M$  is the total magnification of system. The image intensity  $I_{dI2}$  under the maximum diffraction condition is therefore

$$I_{dI2} = \eta_p \frac{B_c}{B_s} \frac{(\text{NA})^2 (f_{21})^2}{(M_1)^4 (M_2)^2 (W_s)^2} I_r, \quad (5)$$

where  $M_2$  is the magnification of the second subsystem.

Photorefractive quantum-well (PRQW) devices are used as our dynamic holographic film.<sup>21-23</sup> The de-

vices can have dust as well as fabrication-induced imperfections that scatter reference light into the direction of the camera and cause diffuse background on the reconstructed image. A scattering efficiency  $\eta_b$  can be introduced to describe the amount of scattering by defects, defined by  $I_b = \eta_b I_0$ , where  $I_b$  is the scattered intensity and  $I_0$  is the incident intensity. When the fraction of the total area of the PRQW device covered by defects is  $A_d$ , the background intensity  $I_{b12}$  at IP2 is

$$I_{b12} \approx \eta_b A_d I_r / \pi (f_{22})^2$$

where  $f_{22}$  is the focal length of lens L22. For the FDH system the signal-to-background (S/B) ratio is therefore

$$S/B = \pi \frac{\eta_p}{\eta_b A_d} \frac{B_c}{B_s} \frac{(NA)^2 (f_{21})^4}{(M_1)^4 (W_s)^2}, \quad (6)$$

To estimate the S/B ratio of the experimental system, it helps to rephrase Eq. (6) in terms of properties of the target, the PRQW device, and the system resolution. The system resolution  $R_s$  is given by  $0.61\lambda/NA$  in the Raleigh criterion, where  $\lambda$  is the wavelength. The numerical aperture in the FDH optical setup is limited by the size of the PRQW device  $W_{PRQW}$  for which

$$NA = M_1 W_{PRQW} / (\sqrt{\pi} f_{21})$$

When the system resolution is expressed as

$$R_s \approx f_{21} \lambda / (M_1 W_{PRQW}), \quad (7)$$

the S/B ratio becomes

$$S/B = \left[ \frac{R(z) \exp(-2\mu'z)}{B_s} \right] \left[ \frac{l_c}{(W_s)^2} \right] \left[ \frac{\eta_p}{\eta_b A_d} \right] \times \left[ \frac{(W_{PRQW})^2 (f_{21})^2}{(M_1)^2} \right]. \quad (8)$$

In Eq. (8), the first term is related to the sample properties, the second term describes the beam properties, the third term is a PRQW property, and the last term is related to the system resolution. The important parameters in Eq. (8), which can be considered for the improvement and maximization of S/B ratio under the constraint of constant system resolution, are  $W_{PRQW}$ ,  $W_s$ ,  $l_c$ , and  $A_d$ . As a qualitative example, if we double the size of the PRQW and double the focal length  $f_{21}$ , the improvement of S/B ratio is 4 times under the same resolution. Similarly, decreasing the beam radius  $W_s$  and increasing the coherence length  $l_c$  improve the S/B ratio, although with a decrease of the field of view and a loss of depth resolution, respectively. These trade-offs can be selected for the needs of different applications.

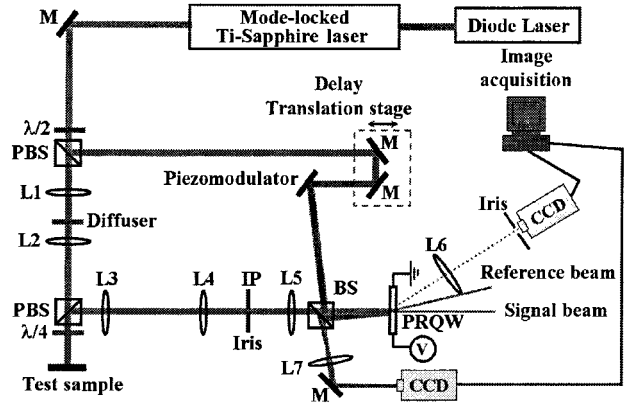


Fig. 2. Experimental setup for FDH; PBSs, polarizing beam splitter; BS, beam splitter; M's, mirrors; L1-L7, lenses;  $\lambda/2$ , half-wave plate;  $\lambda/4$ , quarter-wave plate; IP, image plane; V, voltage.

As a quantitative example, we used device PLO9 with a 3-mm window width as the PRQW device for the experiments in Section 4. The diffraction efficiency of PLO9 device was measured to be  $3 \times 10^{-3}$  for an applied field of 10 kV/cm and a fringe spacing of 12  $\mu\text{m}$  at the wavelength of 839 nm under cw operation of a mode-locked laser. The scattering efficiency  $\eta_b$  of defects in the PLO9 device was measured to be  $4.5 \times 10^{-2}$ , and the total area of defects was measured to be 0.2  $\text{mm}^2$ . The focal length  $f_{21}$  was 4.2 cm, and the magnification of the first subsystem was equal to unity. The calculated transverse resolution for this system was 12  $\mu\text{m}$ , which agreed with measurements through the holographic image of a specular test chart by use of a vibrating diffuser. The depth resolution was measured to be approximately 25  $\mu\text{m}$  by placement of a mirror at the sample position. The incoming signal beam radius was approximately 400  $\mu\text{m}$ , and the intensity was 10  $\text{W}/\text{cm}^2$ . For a diffuse paper target under cw operation of the laser, the value of  $B_c/B_s$  is unity. Therefore, the value of the S/B ratio for a diffuse target under cw operation was estimated to be 90 dB with the use of measured parameters. The measured value of the S/B ratio was 76 dB by direct comparison of the diffracted intensities with background intensities for a diffuse paper target under cw operation. The measured value was a factor of 5 smaller than the calculated one, likely related to optimization and nonunity modulation index. The S/B ratio under mode-locked operation of a mode-locked laser should be smaller than for cw operation because the value of  $B_c/B_s$  is smaller than unity. It should be emphasized that signal-to-noise ratio can be significantly larger than S/B ratio because the background is mostly static scatter and can be subtracted from the images. We show in Section 4 that we reach a -95 dB reflectance limit under mode-locked operation.

### 3. Experimental Performance for Diffuse Test Targets

We used the experimental setup shown in Fig. 2 to record and reconstruct holograms in the PRQW devices, using a mode-locked Ti:sapphire laser (120-fs

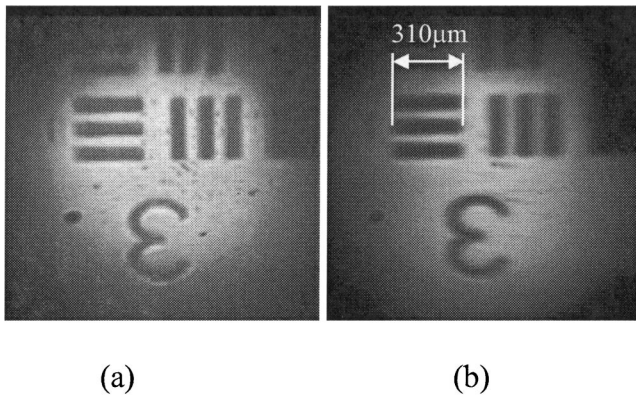


Fig. 3. Background-subtracted holographic images of the USAF test chart obtained with the mode-locked laser (a) under cw operation and (b) under mode-locked operation. Images are obtained through the PRQW device with a 5-mm window size and the lens L5 with a 10-cm focal length by use of a vibrating diffuser.

pulse duration 100-MHz repetition rate) pumped by a diode laser. The wavelength of the laser was tuned to the exciton peak (836 nm) with a bandwidth of 35 nm for the mode-locked laser. The output beam from the laser passed through a first polarizing beam splitter (PBS) to produce a signal and a reference beam. The half-wave plate before the first PBS gave the reference beam a horizontal polarization and the signal beam a vertical polarization. The signal beam passed through a demagnifying telescope that consists of the lens L1 and L2 and passed the second PBS. A quarter-wave plate behind the second PBS ensured that the backscattered signal beam had horizontal polarization after returning through the quarter-wave plate. After the backscattered signal beam passed the second PBS, this signal beam was relayed with a 1:1 magnification by lenses L3 and L4. The lens L5 performed the Fourier transform of the signal beam located at the PRQW device, where it interfered with the reference beam that passed through the delay stage. A vibrating mirror, which was controlled by a piezomodulator in the reference arm, was used to time-average interpixel laser speckle. Fringes from the interference between the signal and the reference beam were recorded on the PRQW device while a 10 kV/cm dc field was applied. The hologram was reconstructed by the +1 or -1 diffraction orders of the reference beam. The diffracted image was viewed through the CCD camera by use of the lens L6. The reconstructed holographic images on the CCD camera were captured by a frame grabber in the computer. Direct images of the image-bearing signal beam were captured by another CCD camera with the lens L7. We used three PRQW devices in this study. Device BH56 and device PLO9 had 3-mm window size, and device JAC63 had a 5-mm window size.

The performance of the FDH system was first evaluated with a specular U.S. Air Force (USAF) test chart, but a vibrating diffuser, which was placed between lens L1 and lens L2, was used to create diffused illumination at the target so that the limitation

of FDH for specular targets (the large intensity variation at the Fourier plane) was eliminated. Figure 3 shows background-subtracted holographic images of the diffusely illuminated USAF test chart. Figure 3(a) was produced under cw operation of a mode-locked laser, and Fig. 3(b) was produced under mode-locked operation of the same laser. These images were obtained through the PRQW device (JAC63) with 5-mm window size, and the focal length of lens L5 was 10 cm. The transverse resolution for this FDH system, calculated with Eq. (7), was  $17\ \mu\text{m}$  and was  $18\ \mu\text{m}$  under cw operation. Under mode-locked operation, the vertical resolution was  $19\ \mu\text{m}$ , and the horizontal resolution was  $35\ \mu\text{m}$ . The measured resolution under cw operation agrees with the calculated value, and the vertical resolution under mode-locked operation closely agrees with the calculated value. However, the horizontal resolution under mode-locked operation is a factor of 2 smaller than the calculated one. This relates to the fringe spacing and the coherence length of the mode-locked laser. If the fringe spacing is small, the area of zero-path-matched signal beam within a coherence length will be small on the PRQW device and hence the resolution will be decreased for a planar target. When the fringe spacing becomes large or the coherence length is extended, the horizontal resolution under mode-locked operation can approach the cw conditions.

#### 4. Experimental Performance for Tumor Spheroids and Mouse Eye

We used rat osteogenic sarcoma tumor spheroids, which are a steady and abundant source of living tissue, for the imaging of biological tissue. To create tumor spheroids, rat osteogenic sarcoma UMR-106 cells were cultured in Dulbecco's modified Eagles' medium in non-tissue-culture plastic dishes. The non-tissue-culture plastic causes the tumor cells to form the spheroids in 7–10 days; the spheroids are then transferred to a rotating bioreactor where they are maintained in suspension. The spheroids were grown up to 1 mm in diameter and are thus large enough to simulate the thickness of different mammalian tissue (skin epidermis is 70–120  $\mu\text{m}$  in thickness over most of the human body). As tumor spheroids are cultured, they undergo cell apoptosis or necrosis in their center and so consist of an inner necrotic core and an outer shell with a 100- to 200- $\mu\text{m}$  thickness of healthy cells.

The FDH system under mode-locked operation was used to obtain stacks of images of the internal structure of tumor spheroids. The data-acquisition method in OCI experiments on living tissue is called a fly-through. We achieved a fly-through on an ordinary video camera by sweeping the reference delay translation stage (Fig. 2). We used a computer-controlled consecutive reference delay with a depth step of  $10\ \mu\text{m}$  ( $7.7\ \mu\text{m}$  in tissue) to acquire a stack of *en face* frames. The time interval between frames is typically 1 s (limited by the data transfer of the current system). Figure 4 shows  $x$ - $y$  sections that were selected per every third frame from a fly-through for a fresh tumor spheroid with a 400- $\mu\text{m}$  diameter. The original

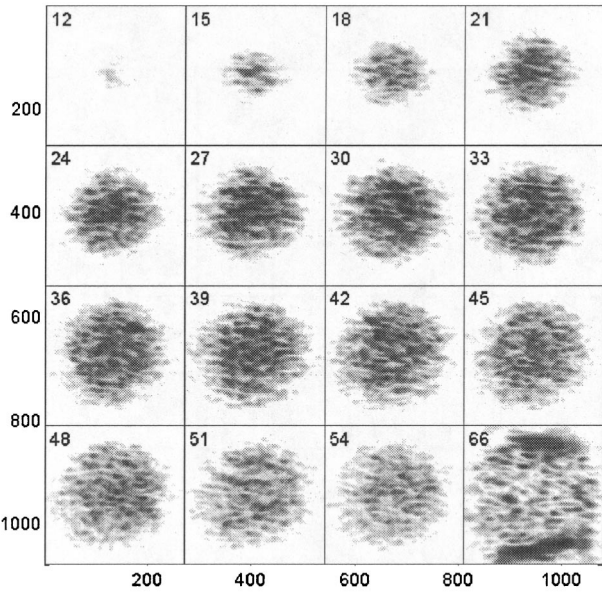


Fig. 4. XY cross section selected per every third frame from fly-through images of a 400- $\mu\text{m}$ -diameter rat osteogenic tumor spheroid. The gray scale is on a logarithmic scale. The petri dish reflection appears in frame 66. Frame 39 is the approximate mid-section.

data set consists of 120 frames of  $400 \times 400$  pixels. The original data were postprocessed by use of direct background subtraction to remove diffuse background. The tumor was in growth medium sitting on the bottom of a petri dish. The petri dish is shown in frame 66, and the top of the tumor is at frame 12 (Fig. 4). The healthy tissue at the top of the tumor presents a dim reflection, whereas the features deeper inside the tumor are brighter, especially at depths near the necrotic core.

The stack of fly-through frames forms a data cube that can be visualized by use of computed reconstruction. Figure 5 shows side views (pseudo-B scans) of the tumor shown in Fig. 4. Cross sections in the  $y$ - $z$  plane are selected out of every 13th from the data cube. The petri dish reflection appears on the right of each frame, and the top of the tumor is on the left in each frame. Frame 136 is the approximate midsection. Stacks of two-dimensional frames can be combined into a volume. A computed three-dimensional volumetric rendering of a 500- $\mu\text{m}$ -diameter tumor spheroid is shown in Fig. 6. The light is incident from the top of the tumor, and the petri dish reflection is at the bottom. The shadow of the tumor is evident on the petri dish. We can estimate the depth of penetration from the dimness of the shadow on the petri dish behind the tumor. The penetration depth into the tumors is currently approximately 0.8 mm. We can adjust the transparency threshold in the computed three-dimensional volumetric rendering to see the different features. In the volumetric rendering of the transparency threshold  $-84$  dB in Fig. 6(a), only the outside healthy shell is shown. When we adjusted to higher transparency thresholds as shown in Fig. 6(b),

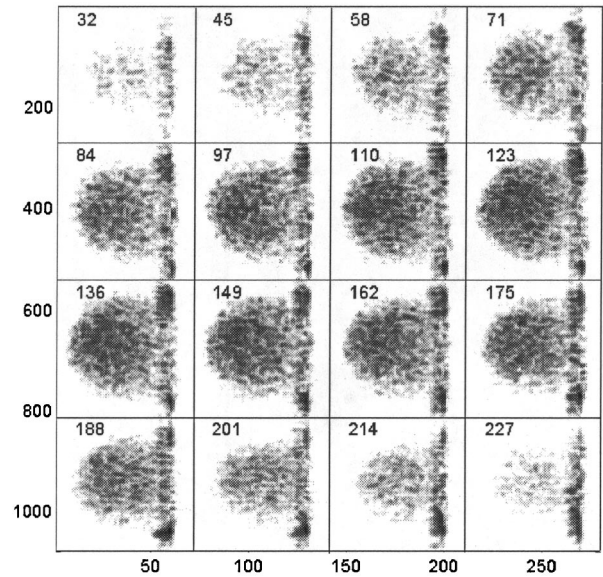


Fig. 5. YZ cross section selected per 13th pixel from fly-through images of the tumor spheroid in Fig. 4. The gray scale is on a logarithmic scale. The petri dish reflection appears on the right of each frame. Frame 136 is the approximate midsection.

6(c), and 6(d), in which the transparency threshold is  $-79$ ,  $-74$ , and  $-69$ , respectively, we observed the bright features inside the tumor, which occur in the necrotic core.

It is important to compare FDH OCI with conventional time-domain OCT. Typical fast-scan OCT systems operate with approximately 110 dB of sensitivity. Figure 7 shows pseudo-A scans (reflectivity versus depth along selected lines) that were selected from the holographic data set shown in Fig. 4. The petri dish reflection is at frame 66, and the top of the tumor spheroid is at frame 12. We can estimate the penetration depth from the noise floor and the slope of the dashed line in Fig. 7. The penetration depth of 0.8 mm was estimated from the dashed-line slope of 66.5 dB/mm and the noise floor of  $-95$  dB. The dynamic range from the tissue is estimated to be approximately 40 dB (see Fig. 7). This performance of FDH OCI in dynamic range is comparable with time-domain OCT. The basic OCI format is a two-dimensional section at a selected depth compared with the single-line (A-scan) format of an OCT scan. The simultaneous acquisition of all pixels in the two-dimensional plane gives OCI a multiplex advantage for signal-to-noise ratio equal to the number of pixels, which is currently  $1.6 \times 10^5$ . This multiplex advantage offsets the diffraction inefficiencies of the holographic film.

The holographic feature intensities for the necrosis are stronger than for the healthy cell because the necrosis produces higher reflection than the healthy cell. The large-size tumors contain more extensive regions of necrosis concentrated toward the center with a shell of rapidly dividing healthy cells near the surface. Smaller tumors contain primarily healthy tumor cells with few necrotic regions and microcalci-

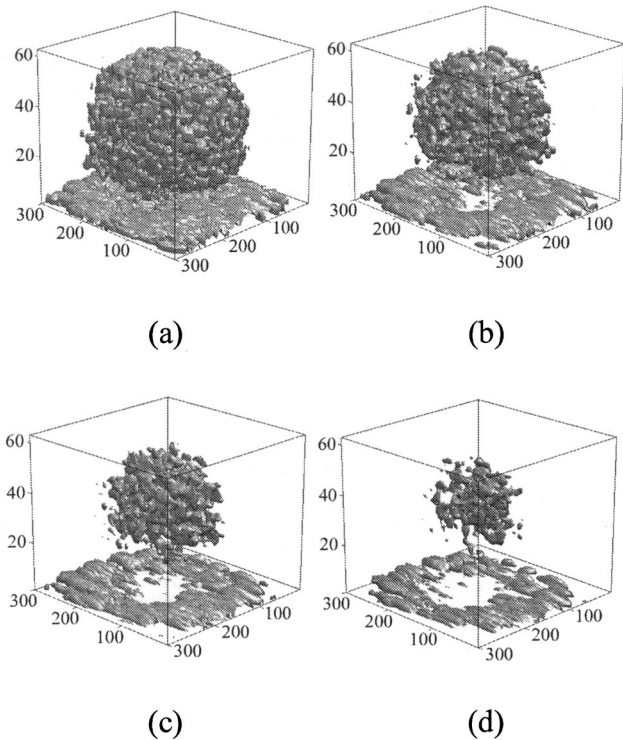


Fig. 6. Volumetric rendering reconstructed by computer from fly-through images of a 500- $\mu\text{m}$ -diameter tumor spheroids. The light is incident from the top, and the petri dish reflection is at the bottom. The shadow of the tumor spheroid is evident on the petri dish. The transparency threshold of  $-84$ ,  $-79$ ,  $-74$ , and  $-69$  dB is adjusted for (a), (b), (c), and (d), respectively, to see the different features inside the tumor.

fications. The difference in the distribution of necrosis can be viewed in the holographic feature intensities. We have analyzed the distribution of necrosis inside four different-size tumors (260, 360, 460, and 560  $\mu\text{m}$ ) by obtaining average intensities of the holographic features as a function of radius from the center of the tumor as shown in Fig. 8. It is clear that feature intensities near the center, which are the region of necrosis, are stronger and that they decrease to smaller values at the tumor surface, which is the region of healthy tumor cells. The difference among the four tumors is the tangential slope, which is consistent with the decreasing necrotic density. The necrotic density for the larger tumor decreases more slowly than for the smaller tumor. These results are significant because they point out that the FDH OCI can differentiate diseased tissues from healthy tissues, which is one of the primary goals of diagnostic imaging.

To show the repeatability of the FDH system, we performed consecutive fly-throughs on a single tumor. The tumor had been polymerized (cross-linked) by the addition of glutaraldehyde. The repeatability of the FDH system was quantified by the cross-correlation analysis shown in Fig. 9. The time interval between two consecutive fly-throughs was 4 min. The cross-linked tumor showed a 98% cross correla-

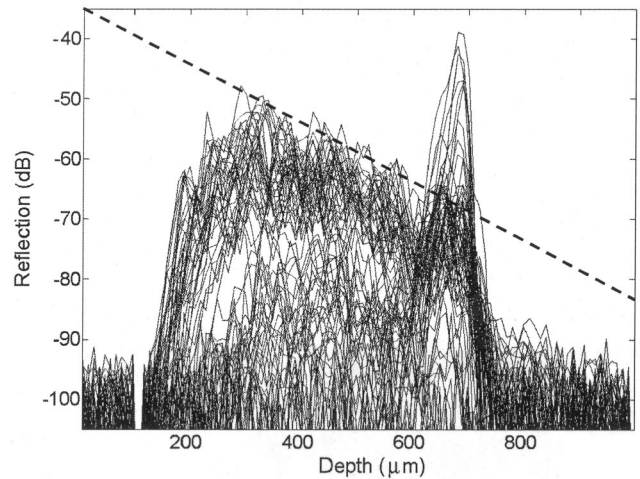


Fig. 7. Pseudo-A scans selected from fly-through images of the tumor spheroid in Fig. 4. The petri dish reflection is at frame 66, and the top of the tumor spheroid is at frame 12. The noise floor is at  $-95$  dB, and the dynamic range is approximately 40 dB. The penetration depth of 0.8 mm is acquired from the dashed-line slope of 66.5 dB/mm.

tion between two consecutive fly-throughs, whereas a fresh tumor showed a 78% cross correlation. A cross correlation of 60% resulted from the cross correlation from random tumors. Cross correlation in the fresh tumor is lower than for the cross-linked tumor because the fresh tumor has the cellular motility of organelles and plasma membranes. From these experiments we rule out any significant system motion. It also demonstrates that the tissue features observed are robust and repeatable, that the sample mounting produces no variability, and that the optical information is not random speckle but is related to specific structure inside the tumor spheroids.

To demonstrate the more general capabilities of the

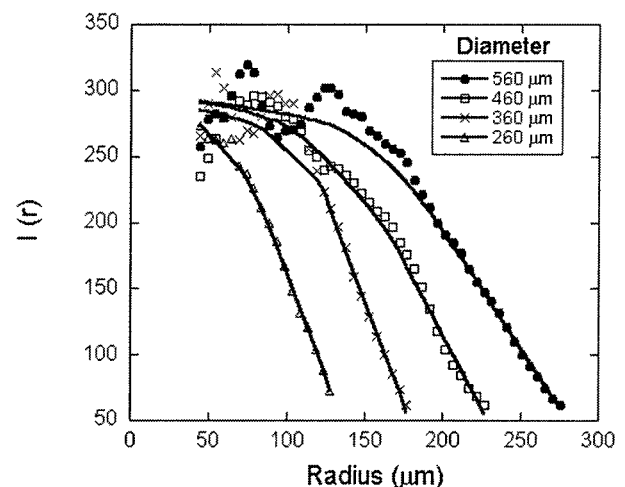


Fig. 8. Average intensities of the holographic features as a function of radius from four different-size tumors. Feature intensities near the center are stronger, and they decrease to small values at the tumor surface, which is consistent with decreasing necrosis density from the center to the surface.

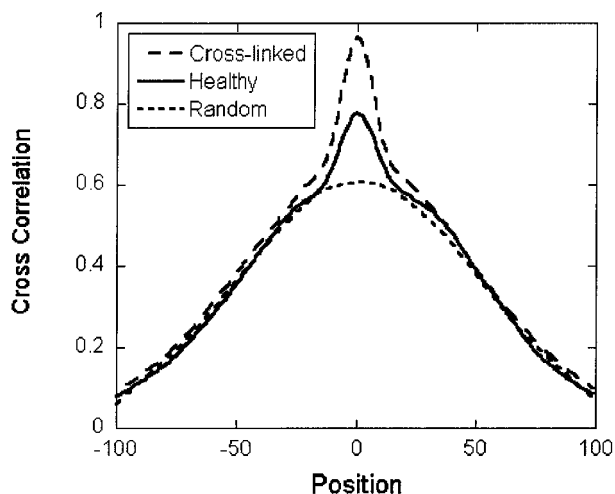


Fig. 9. Cross-correlation functions from two consecutive fly-throughs of the same cross-linked tumor and the same healthy tumor. Cross-correlation function for random tumor was obtained from fly-throughs of two random tumors.

holographic approach to imaging diverse tissue, we performed a fly-through of a cross-linked mouse eye. From the fly-through data cube we extracted the section shown in Fig. 10. The section shows parts of the cornea, the iris, and the lens in the mouse eye. The anterior chamber cornea-iridial angle is clearly observed with an angle of  $18^\circ$ . The anterior chamber angle is an important indicator of glaucoma but is difficult to measure with conventional techniques. The relatively strong reflections from the transparent cornea and lens demonstrate the strong sensitivity achievable with FDH OCI.

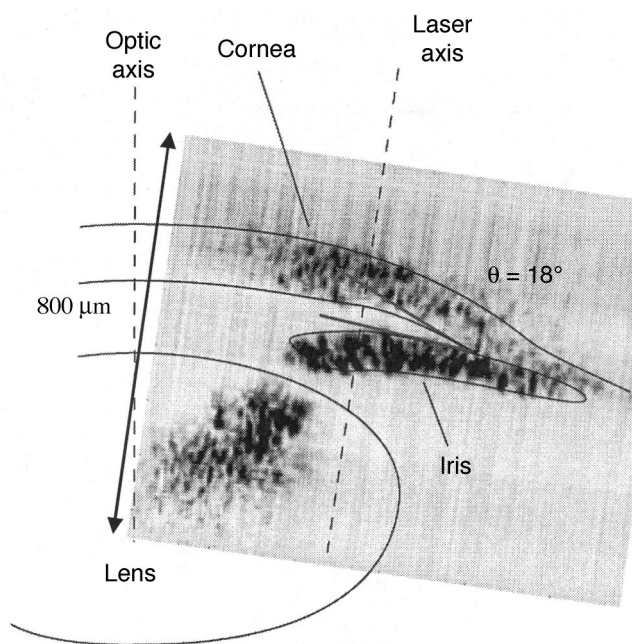


Fig. 10. Midsection extracted from the holographic fly-through images of a mouse eye. The anterior chamber cornea-iridial angle is clearly observed.

## 5. Discussion

We have explored FDH in PRQW devices in a high-dynamic-range OCI technique. We demonstrate that the ability to use FDH is enhanced by the use of a diffuse target, such as scattering tissue, rather than specular targets. By analysis of FDH and use of measured parameters, we show that the S/B ratio in cw operation can reach 90 dB. We present, to our knowledge, the first results of FDH applied to OCI of tissue. We show improved performance for Fourier-domain OCI on rat osteogenic sarcoma tumor spheroids and mouse eye that provides significantly better image quality and higher dynamic range than is possible with IDH. We make the experimental demonstration of  $-95$ -dB sensitivity and  $40$ -dB dynamic range from tissue for FDH OCI, which is comparable with fast-scan time-domain OCT system sensitivities. We also demonstrate that FDH OCI has good repeatability and can differentiate diseased tissues from healthy tissues, which is one of the primary goals of diagnostic imaging. To these ends, further improvement in the dynamic range and resolution are anticipated as the technology of PRQW devices matures.

This research was supported by the National Science Foundation under grant BES-0401858.

## References

1. R. C. Youngquist, S. Carr, and D. E. N. Davies, "Optical coherence-domain reflectometry: a new optical evaluation technique," *Opt. Lett.* **12**, 157–160 (1987).
2. E. A. Swanson, D. Haung, M. R. Hee, and J. G. Fujimoto, "High-speed optical coherence domain reflectometry," *Opt. Lett.* **17**, 151–153 (1992).
3. S. C. W. Hyde, N. P. Barry, R. Jones, J. C. Dainty, P. M. W. French, M. B. Klein, and B. A. Wechsler, "Depth-resolved holographic imaging through scattering media by photorefraction," *Opt. Lett.* **20**, 1331–1333 (1995).
4. S. C. W. Hyde, R. Jones, N. P. Barry, J. C. Dainty, P. M. W. French, K. M. Kwolek, D. D. Nolte, and M. R. Melloch, "Depth-resolved holography through turbid media using photorefraction," *IEEE J. Sel. Top. Quantum Electron.* **2**, 965–975 (1996).
5. R. Jones, S. C. W. Hyde, M. J. Lynn, N. P. Barry, J. C. Dainty, P. M. W. French, K. M. Kwolek, D. D. Nolte, and M. R. Melloch, "Holographic storage and high background imaging using photorefractive multiple quantum wells," *Appl. Phys. Lett.* **69**, 1837–1839 (1996).
6. R. Jones, N. P. Barry, S. C. W. Hyde, P. M. W. French, K. M. Kwolek, D. D. Nolte, and M. R. Melloch, "Direct-to-video holographic readout in quantum wells for 3-D imaging through turbid media," *Opt. Lett.* **23**, 103–105 (1998).
7. M. Tziraki, R. Jones, P. M. W. French, M. R. Melloch, and D. D. Nolte, "Photorefractive holography for imaging through turbid media using low coherence light," *Appl. Phys. B* **70**, 151–154 (2000).
8. D. Huang, E. A. Swanson, C. P. Lin, J. S. Schuman, W. G. Stinson, W. Chang, M. R. Hee, T. Flotte, K. Gregory, C. A. Puliafito, and J. G. Fujimoto, "Optical coherence tomography," *Science* **254**, 1178–1181 (1991).
9. M. R. Hee, J. A. Izatt, J. M. Jacobson, J. G. Fujimoto, and E. A. Swanson, "Femtosecond transillumination optical coherence tomography," *Opt. Lett.* **18**, 950–952 (1993).
10. J. M. Schmitt, "Optical coherence tomography (OCT): a review," *IEEE J. Sel. Top. Quantum Electron.* **5**, 1205–1215 (1999).

11. Z. Ansari, Y. Gu, J. Siegel, D. Parsons-Karavassilis, C. W. Dunsby, M. Itoh, M. Tziraki, R. Jones, P. M. W. French, D. D. Nolte, W. Headley, and M. R. Melloch, "High-frame-rate, 3-D photorefractive holography through turbid media with arbitrary sources and photorefractive structured illumination," *IEEE J. Sel. Top. Quantum Electron.* **7**, 878–886 (2001).
12. C. Dunsby, Y. Gu, Z. Ansari, P. M. W. French, L. Peng, P. Yu, M. R. Melloch, and D. D. Nolte, "High-speed depth-sectioned wide-field imaging using low-coherence photorefractive holographic microscopy," *Opt. Commun.* **219**, 87–99 (2003).
13. P. Yu, M. Mustata, P. M. W. French, J. J. Turek, M. R. Melloch, and D. D. Nolte, "Holographic optical coherence imaging of tumor spheroids," *Appl. Phys. Lett.* **83**, 575–577 (2003).
14. P. Yu, M. Mustata, L. Peng, J. J. Turek, M. R. Melloch, P. M. W. French, and D. D. Nolte, "Holographic optical coherence imaging of rat osteogenic sarcoma tumor spheroids," *Appl. Opt.* **43**, 4862–4873 (2004).
15. P. Yu, L. Peng, M. Mustata, J. J. Turek, M. R. Melloch, and D. D. Nolte, "Time-dependent speckle in holographic optical coherence imaging and the health of tumor tissue," *Opt. Lett.* **29**, 68–70 (2004).
16. E. N. Leith and J. Upatnieks, "Wavefront reconstruction with diffused illumination and three-dimensional objects," *J. Opt. Soc. Am.* **54**, 1295–1301 (1964).
17. G. W. Stroke, D. Brumm, and A. Funkhouser, "Three-dimensional holography with "lensless" Fourier-transform holograms and coarse p/n Polaroid film," *J. Opt. Soc. Am.* **55**, 1327–1328 (1965).
18. W. S. Haddad, D. Cullen, J. C. Solem, J. W. Longworth, A. McPherson, K. Boyer, and C. K. Rhodes, "Fourier-transform holographic microscope," *Appl. Opt.* **31**, 4973–4978 (1992).
19. R. Jones, N. P. Barry, S. C. W. Hyde, M. Tziraki, J. C. Dainty, P. M. W. French, D. D. Nolte, K. M. Kwolek, and M. R. Melloch, "Real-time 3-D holographic imaging using photorefractive media including multiple-quantum-well devices," *IEEE J. Sel. Top. Quantum Electron.* **4**, 360–369 (1998).
20. K. Jeong, L. Peng, D. D. Nolte, and M. R. Melloch, "Fourier-domain holography in photorefractive quantum-well films," *Appl. Opt.* **43**, 3802–3811 (2004).
21. D. D. Nolte, D. H. Olson, G. E. Doran, W. H. Knox, and A. M. Glass, "Resonant photodiffractive effect in semi-insulating multiple quantum wells," *J. Opt. Soc. Am. B* **7**, 2217–2225 (1990).
22. D. D. Nolte and M. R. Melloch, "Photorefractive quantum wells and thin films," in *Photorefractive Effects and Materials*, D. D. Nolte, ed. (Kluwer Academic, Dordrecht, The Netherlands, 1995), pp. 373–451.
23. D. D. Nolte, "Semi-insulating semiconductor heterostructures: optoelectronic properties and applications," *J. Appl. Phys.* **85**, 6259–6289 (1999).